Taylor & Francis
Taylor & Francis Group

Stereo cloud-top heights and cloud fraction retrieval from ATSR-2

J.-P. MULLER*†‡, M.-A. DENIS†§, R. D. DUNDAS†¶, K. L. MITCHELL†**,
C. NAUD†*** and H. MANNSTEIN****

†Department of Geomatic Engineering, University College London (UCL), Gower
Street, London WC1E 6BT, UK
‡now at Department of Space and Climate Physics, MSSL, UCL, Holmbury St. Mary,
Dorking, Surrey, RH5 6NT, UK
§now at Groupe On-X, Division Technologies, 15 quai de Dion Bouton, 92816 Puteaux
Cedex, France
¶now at Office for National Statistics, 1 Drummond Gate, London SW1V 2QQ, UK
**now at Mail Stop 183-601, Jet Propulsion Laboratory, 4800 Oak Grove Drive,
Pasadena, CA, 91109-8099, USA
***Columbia University, NASA – Goddard Institute for Space Studies, 2880 Broadway,
Room 678, New York, NY 10025, USA
****Deutsches Zentrum für Luft- und Raumfahrt, Institut für Physik der Atmosphäre,
Oberpfaffenhofen, D – 82234 Wessling, Germany

An operational processing system is described for the automated retrieval of
cloud-top heights (CTHs) and amounts from the Gridded Brightness
Temperature (GBT) 1 km product derived from the dual view of the Along
Track Scanning Radiometer (ATSR-2) instrument onboard the ESA ERS-2
satellite. A new stereo matching algorithm, called M4 is described together with
the overall processing chain for retrieving cloud-top heights and amounts. M4 is
based on the successful stereo matchers, M2 and M3 which have been in
operation with the NASA MISR sensor since March 2000 and which have also
been applied to mapping cloud fraction in the polar region using ATSR-2
(Cawkwell and Bamber 2002, Cawkwell *et al.* 2001). Results in companion
papers (Naud *et al.*, Denis *et al.* 2007) describe the accuracy achieved using this
algorithm and detailed scene-by-scene results are available from http://
cloudmap.org under results->UCL->ATSR-2 Validation. We assess the impact
of cloud-top winds on the accuracy of the retrieved cloud-top heights and
conclude that for most middle and lower tropospheric clouds, cloud-top winds
will have little, if any, noticeable impact. We show how ATSR-2 cloud-top
heights at the different wavelengths (particularly visible compared with thermal
IR) can sometimes yield information on multi-layer clouds which is unique to
ATSR-2. The processing system has recently been applied to three years of
ASTR-2 GBT data and results are shown. These results are available from the
British Atmospheric Data Centre (http://badc.nerc.ac.uk/data/list_all_datasets.
html?source=data).

*Corresponding author. Email: jpm@mssl.ucl.ac.uk

1. Introduction

The Along-Track Scanning Radiometer 2 (ATSR-2) is a precision imaging radiometer instrument based on its forerunner, the ATSR (Mutlow *et al.* 1994). It was launched in 1995 onboard the second European Remote-Sensing Satellite, ERS-2. It has three infrared (IR) channels (at 3.7μm, 10.85μm and 12μm) and four visible/near-infrared channels (0.55μm, 0.659μm, 0.87μm and 1.6μm). Only three spectral bands are considered here (wavelengths centred at 0.659μm, 1.6μm, and 10.85μm hereafter referred to as 11.0μm, respectively) as previous experiments (not shown here) have shown these are the only ones to yield unique information on cloud-top heights for use in meteorology. The other bands did not show any significant differences to these four bands. The principles of operation and how these are used for stereo photogrammetric retrieval are described in a companion paper (Denis *et al.* 2007).

Stereo photogrammetric techniques represent the only independent method for cloud-top height retrieval in passive remote sensing. They are independent in that they do not rely on ancillary data such as objective analyses of temperature-pressure profiles. However, prior to ATSR in 1991 stereoscopic observations were only available for limited campaign experiments using either overlapping simultaneous geostationary visible data (as Infrared observations suffer from too low a resolution) or specific polar-orbiting coincidences with geostationary satellite observations (Black 1983, Fujita 1982, Fujita and Dodge 1983, Hasler 1981a, Hasler 1981b, Hasler *et al.* 1983, Hasler *et al.* 1991, Lorenz 1983, Mack *et al.* 1982, Mack *et al.* 1983a, Mack *et al.* 1983b, Mahani *et al.* 2000, Minzer *et al.* 1978, Mosher 1976, Mosher and Young 1983, Rodgers *et al.* 1983a, Rodgers *et al.* 1983b, Shenk *et al.* 1975, Szejwach *et al.* 1983, Takashima *et al.* 1982, Warner *et al.* 1973, Whitehead *et al.* 1969, Wylie *et al.* 1998). As the technology matures and geostationary satellite radiometers achieve similar resolutions to polar-orbiters, (around 1 km in the Infrared), they represent an alternative and complementary method for obtaining near-global cloud-top heights, winds and cloud fractions to brightness temperature methods, such as CO_2-slicing (Wielicki and Coakley 1981) and more recent methods such as Oxygen A-band (Preusker *et al.* 2007). Prior to the launch of ERS-1 with the ATSR instrument, Lorenz (1985) proposed the usage of this instrument for stereoscopic cloud height and wind retrievals.

ATSR and ATSR-2 represent with the follow-on AATSR sensor onboard the ESA ENVISAT, a potential for up to 15-plus years of continuous measurement of cloud-top heights and amounts. One of the greatest current uncertainties in Global Climate Models as highlighted in the 3rd IPCC Assessment (Houghton *et al.* 2001) is the net effect of clouds on the Earth's radiation balance, particularly Cirrus and Marine Strato-Cumulus (StCu), especially with regards whether clouds will enhance or decrease the effects of global warming.

In a review of existing surface and satellite-based cloud climatologies (Norris 2000) surface observations of cloud cover, optimized for low clouds, were compared with satellite observations, biased for higher clouds (from the International Satellite Cloud Climatology Program, ISCCP, Rossow and Schiffer 1991, Schiffer and Rossow 1983) from the same time period (1984–1993). The inter-comparison indicated that surface observations of clouds had an opposite trend to satellite observations. Norris also found that there were artefacts in both sets of observations with ISCCP being partly contaminated by the footprint of geostationary observations.

An alternative cloud climatology produced by Wylie and Menzel (1999) from HIRS CO2-slicing observations from the NOAA satellites showed different cloud fractions for high clouds, especially thin semi-transparent clouds compared with ISCCP for 8 years of observations. More recent results (P. Menzel, private communication, 2004) indicates that this difference (HIRS-ISCCP) for high cloud fractions is as much as 10% over land and ocean with the ISCCP data indicating a lowering of high cloud fraction and the HIRS data indicating no such trend over an even longer time period (1978–2001). Inter-comparisons of the NASA MODerate resolution Imaging Spectrometer, MODIS (CO_2 slicing such as HIRS, see King *et al.* 1992) and the NASA Multi-angular Imaging SpectroRadiometer, MISR (stereo) show that different cloud-top heights are often detected at different wavelengths and view angles (Naud *et al.* 2002) and recent results from the NASA Shuttle experiment (Lancaster *et al.* 2003) show that this is also the case for thermal IR stereo cloud-top heights compared with near-IR lidar results. ATSR-2 (and its follow-on AATSR) therefore appears to represent an unique opportunity to compare and assess cloud-top heights derived from stereo at multispectral wavelengths and using radiometric look-up table methods based on brightness temperatures (e.g. Saunders 1988). However, such an assessment is still ongoing and is not reported here. In the next section, the overall ATSR-2 processing chain is described. This is followed by a detailed description of the new stereo matcher and a comparison of results for ATSR-2 with the M2/M3 matchers used for MISR operational processing. The following section shows what impact, if any, wind advection has on cloud-top height accuracy whilst the next section describes some results of applying the cloud-top height system for the retrieval of multi-layer cloud information when the upper cloud layer is sufficiently thin. The final section discusses the results and overall conclusions.

2. ATSR-2 processing chain

An IDL processing chain has been created which extracts three spectral channels (0.65, 1.6 and 11μm) from the ATSR-2 GBT product at 1 km and creates user-selectable cloud-top height and cloud fraction based on either M2/M3 or M4 stereo matcher (see below), using either of the two camera models (see Denis *et al.* 2007). The various processing steps are illustrated schematically in figure 1 (*a*, *b*). The key stages of the entire processing chain can be summarized as follows:

1. Ingest GBT product and select the three spectral bands (11μm, 1.6μm and 0.65μm) and two looks as well as the relevant georeferencing information and camera information (see Denis *et al.* 2007 for more details).
2. Select and apply relevant stereo matcher (M2/M3 or M4) to produce Digital Disparity Models (DDMs) which provide along-track (y) and across-track (x) disparity values.
3. Use camera model to space intersect projected rays from the two looks to find the point of closest perpendicular distance (minimum skewness) using camera model (loc. cit.) and provide elevation values above the reference ellipsoid (WGS84) for these disparity values to create a Digital Disparity and Elevation Model (DDEM) array (this and the following three steps are all shown in figure 1(*a*)).
4. The cloud mask is calculated in two stages: by comparing the DDEM elevation values with a ground Digital Elevation Model (DEM) (provided by NGA, called the Digital Terrain and Elevation Data level 0, DTED0,
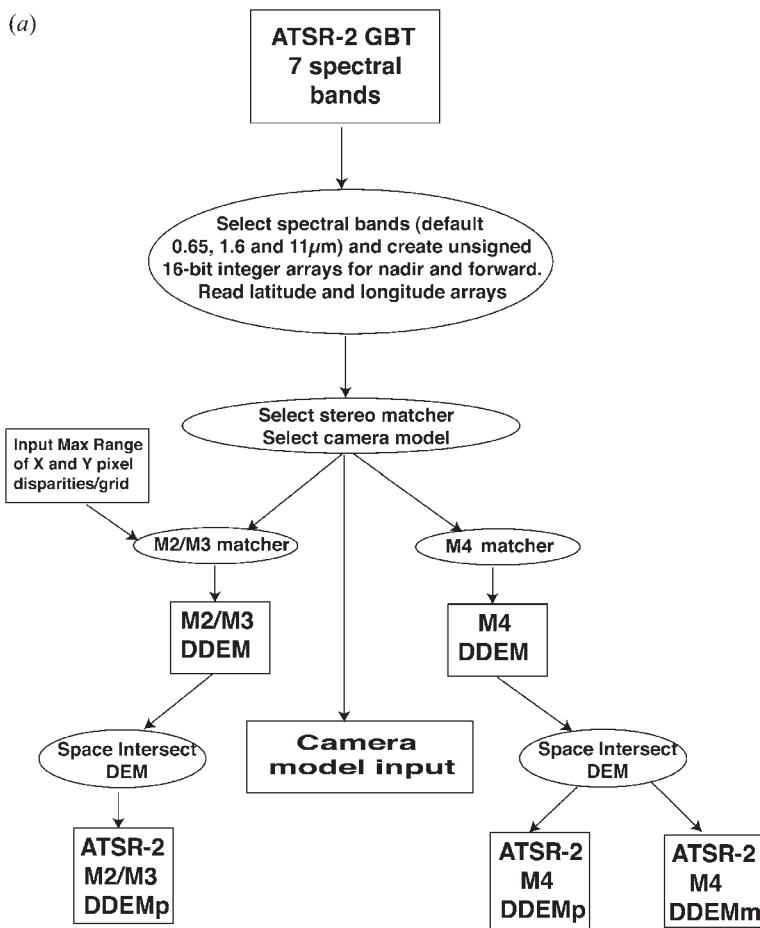
(*a*)

Figure 1. (*a*) Processing chain for disparity retrieval from ATSR-2 GBT processing chain. The camera models are described further in Denis *et al.* (2007) (*b*) Processing chain for calculation of cloud-top heights and cloud fractions from stereo disparities. See text for explanation of acronyms.

originally at a grid-spacing of 30 arc-seconds, $\approx$1 km) and then applying a 1 km height threshold to eliminate potential contamination from ground DEM pixels. This stereo-derived cloud mask is then provided together with the radiance cloud mask to produce a composite cloud mask (see figure 1(*b*)).

5. Only extreme wind conditions are taken into account in the processing chain using the same conditions (x-disparity standard deviation >3 pixels) proposed by Prata and Turner (1997).

The total processing time for the ATSR-2 processssing chain for an 11 MB 5-channel input (only 3 of which are matched) producing a 3-channel CTH and cloud fraction output (of 4.8 Mbytes) takes approximately 15 minutes on a low-specification (1 GHz) PC-Intel processor.

3. M4 stereo matcher

Although the M4 matcher is an area-based stereo matcher like the Multi-point Matcher (M2) and the Multi-point Matcher using Medians (M3), it is based on a
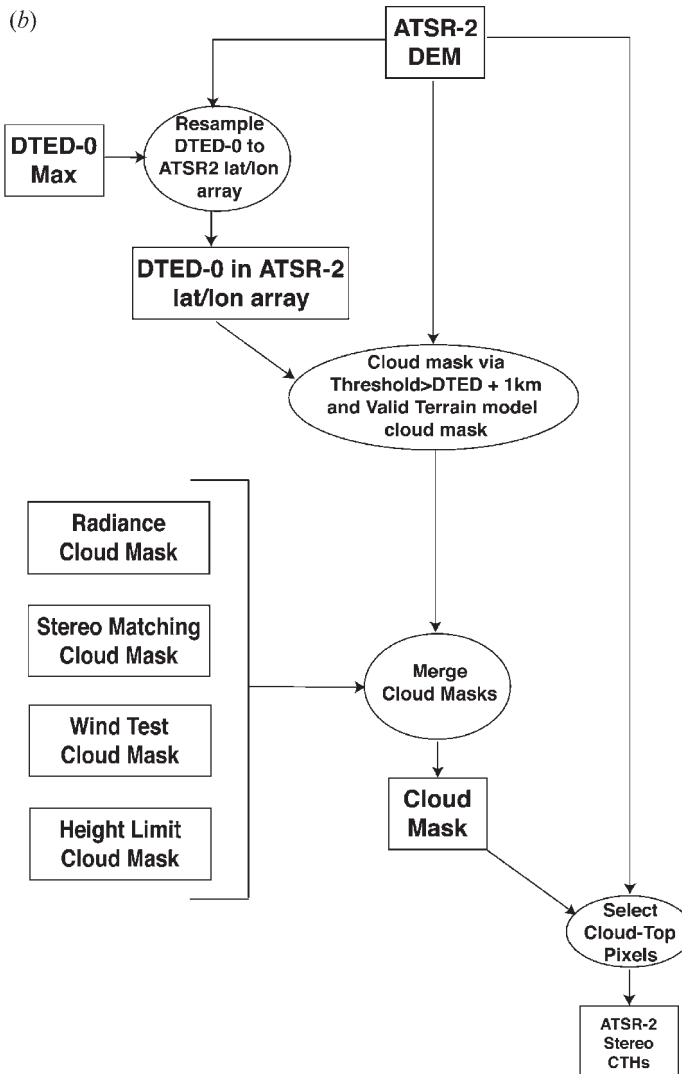
(*b*)

Figure 1. Continued.

different approach to M2/M3 described in Muller *et al.* (2002). The increased speed and coverage of this matcher arises from applying highly optimised image processing routines such as the Fourier transform or convolution coded in IDL. As far as possible, rotational symmetric, smooth filters and templates developed for the DLR contrail detection algorithm (Mannstein 1999) are used to avoid the dominance of signals along the image diagonals. It also includes an automated calculation of the search window prior to the computation of disparities and the use of a quality test.

3.1 *Normalization*

To minimize high computational loads, the first step of the M4 matcher is the application of an adaptive regional highpass filter to normalise the two 2-dimensional arrays, the reference and the comparison images whose sizes are define by (xsize × ysize).

The filter is based on the convolution of both data arrays (e.g. initial images) with a rotational symmetric Gaussian shaped kernel of a specified width:

$$\text{Ke}\left(x_j, y_k\right) = \frac{\frac{1}{\sqrt{2\pi}\sigma} e^{\frac{-d_{j,k}^2}{2\sigma^2}}}{\sum\limits_{d_{j,k}} \frac{1}{\sqrt{2\pi}\sigma} e^{\frac{-d_{j,k}^2}{2\sigma^2}}}. \tag{1}$$

The kernel size $(p \times q)$ and the standard deviation σ are by default set equal to 21×21 pixel and $\frac{21}{4}$, respectively. The distance $d_{j,k}$ is computed using the equation:

$$d_{j,\,k}^2 = x_j^2 + y_k^2, \tag{2}$$

where $x_j \in \left[-\frac{p-1}{2}, \frac{p-1}{2}\right]$ and $y_k \in \left[-\frac{q-1}{2}, \frac{q-1}{2}\right]$.

In the M4 matcher the lowpass filtered reference image is computed by convolving the reference image with the Gaussian shaped kernel:

$$R_{Ke} = R \bullet Ke, \tag{3}$$

e.g.:

$$R_{Ke}\left(x_j, y_k\right) = \begin{cases} \sum\limits_{m=0}^{p-1} \sum\limits_{n=0}^{q-1} R\left(x_j + m - \frac{p}{2}, y_k + n - \frac{q}{2}\right) \times Ke(m, n) \\ \qquad \text{if } \left(\frac{p}{2} < x_j < \text{xsize} - \frac{p}{2}\right) \text{ and } \left(\frac{q}{2} < y_k < \text{ysize} - \frac{q}{2}\right), \\ 0 \quad \text{otherwise} \end{cases} \tag{4}$$

and the regional standard deviation is defined by the formula:

$$\sigma_{\text{M4, R}} = \sqrt{\left(R - R_{Ke}\right)^2 \bullet Ke}, \tag{5}$$

e.g.:

$$\sigma_{\text{M4},R}\left(x_j, y_k\right) = \begin{cases} \sqrt{\sum\limits_{m=0}^{p-1} \sum\limits_{n=0}^{q-1} \left(R - R_{Ke}\right)^2 \left(x_j + m - \frac{p}{2}, y_k + n - \frac{q}{2}\right) \times Ke(m, n)} \\ \qquad \text{if } \left(p \leq x_j \leq \text{xsize} - p\right) \text{ and } \left(q \leq y_k \leq \text{ysize} - q\right) \\ 0 \quad \text{otherwise} \end{cases}, \tag{6}$$

The normalization of the reference image with the adaptive highpass filter used by M4 is obtained by dividing the difference of this image to the lowpass filtered reference image by the regional standard deviation, $\sigma_{\text{M4,R}}$:

$$R_{\text{norm}}\left(x_j, y_k\right) = \frac{R\left(x_j, y_k\right) - R_{Ke}\left(x_j, y_k\right)}{\sigma_{\text{M4},R}\left(x_j, y_k\right) + \varepsilon}, \tag{7}$$

for $(p \leqslant x_j \leqslant \text{xsize} - p)$ and $(q \leqslant y_k \leqslant \text{ysize} - q)$ and where $R(x_j, y_k)$ and $R_{Ke}(x_j, y_k)$ are the Bi-directional Reflectance Factor (BRF) or the brightness temperatures of the reference image pixel value and of the lowpass filtered reference image pixel value at (j, k), respectively. The small positive number ε is set here to avoid zero divisions and to limit the amplification of image noise. Its default value is set equal to 10^{-3}. M4 is computed on the whole image simultaneously and the kernels are used to localize quantities.

The normalization of the comparison image C yields a similar set of equations:

$$C_{norm}(x_j, y_k) = \frac{C(x_j, y_k) - C_{Ke}(x_j, y_k)}{\sigma_{M4,C}(x_j, y_k) + \varepsilon}, \qquad (8)$$

for $(p \leqslant x_j \leqslant xsize - p)$ and $(q \leqslant y_k \leqslant ysize - q)$ and where C_{norm} is the normalised comparison image. C_{Ke} and $\sigma_{M4, C}$ are the lowpass filtered comparison image and the regional standard deviation, respectively and are given by the following equations:

$$C_{Ke}(x_j, y_k) = \begin{cases} \sum_{m=0}^{p-1} \sum_{n=0}^{q-1} C\left(x_j + m - \frac{p}{2}, y_k + n - \frac{q}{2}\right) \times Ke(m, n) \\ \qquad \text{if } \left(\frac{p}{2} < x_j < xsize - \frac{p}{2}\right) \text{ and } \left(\frac{q}{2} < y_k < ysize - \frac{q}{2}\right), \\ 0 \quad \text{otherwise} \end{cases} \qquad (9)$$

and:

$$\sigma_{M4,C}(x_j, y_k) = \begin{cases} \sqrt{\sum_{m=0}^{p-1} \sum_{n=0}^{q-1} (C - C_{Ke})^2\left(x_j + m - \frac{p}{2}, y_k + n - \frac{q}{2}\right) \times Ke(m, n)} \\ \qquad \text{if } (p \leq x_j \leq xsize - p) \text{ and } (q \leq y_k \leq ysize - q) \\ 0 \quad \text{otherwise} \end{cases} \qquad (10)$$

The small positive value ε and the Gaussian shaped kernel Ke used here have the same default values as for the normalization of the reference image.

Note that both normalizations are not carried out at the edges of the initial images and to avoid very high spatial frequencies the normalized values are limited to the range of $[-2, 2]$. The size of the neglected edges is currently set to the size of the Gaussian shaped kernel.

In comparison to the M2 matcher, for which the normalization of the reference image within a square target patch is given by the formula:

$$R_{norm, M2}(x_j, y_k) = \frac{R(x_j, y_k) - \langle R \rangle}{R_{max} - R_{min}}, \qquad (11)$$

where $\langle R \rangle$, R_{max} and R_{min} are the average, the maximum and the minimum BRF or temperature values within the target patch, respectively M4 does not use this approach. Avoiding these steps makes the M4 matcher less computational expensive and thus much faster.

3.2 Determination of the search window

The M4 matcher is an area-based stereo matcher but unlike others (for example, the M2 and M3 matchers), it can automatically perform the calculation of the search window size using information obtained during the acquisition of all possible disparities. The computation of displacement vectors between the normalized reference and comparison images is based on a cross-correlation method. This method is optimized by the application of fast Fourier transforms.

The cross-correlation between the normalized reference and comparison images:

$$corr(u, v) = \sum_{j, k} R_{norm}(x_j, y_k) \times C_{norm}(x_j - u, y_k - v), \qquad (12)$$

is obtained by multiplying the Fourier transform of the first image with the conjugate complex of the Fourier transform of the second one and performing the backward transform of the product:

$$\text{corr}(u, v) = F^{-1}(F(R_{norm})F^*(C_{norm})), \qquad (13)$$

where the function F and the symbol * designate the Fourier transform and the conjugate complex value of it, respectively. R_{norm} and C_{norm} refer to the normalized reference and the comparison images, respectively.

One should note that applying the cross-correlation to the initial, not normalised reference and comparison images does not work because the image edges and some large-scale features dominate the cross-correlation rather than the local image texture or contrast.

The cross-correlation is therefore performed using the whole normalized images. As long as there are no major regular structures, most parts of the images are uncorrelated for a certain disparity. Relevant high values of the cross-correlation map correspond to possible displacement vectors (u, v). In order not to miss any of these, the result of the cross-correlation is smoothed with a 3×3 moving average filter. To avoid edge effects while applying the filter, the zero point of the correlation map is shifted to the centre prior to the smoothing and shifted back to zero again afterwards.

The resulting values are sorted by descending order and the highest values are selected. The default is to select all values higher than the value of the 95% percentile. The motivation behind this is that most of the cross-correlation values are close to zero and this 'noise' is evenly distributed. With the value of the 95% percentile the width of this distribution is estimated and only values higher than this width, e.g. values above the noise, are considered as useful.

The result of the cross-correlation provides a search window for each and every image pixel with only a small local window needed to calculate local disparities. The total number of possible displacement vectors is currently limited to a value of 500, which would be reached with a search window of 20×25 pixels. Using the method implemented in the M4 matcher the search window, that has to be predefined in other matchers, is now replaced by an ordered list of possible displacement vectors resulting from the cross-correlation of the normalized images.

3.3 *Computation of the local displacement vectors*

Each displacement vector from the aforementioned list (*i.e.* from the disparity that causes the maximum cross-correlation value until the last one above the 95% percentile) is now used to shift back the whole normalized comparison image (In M4, due to the ATSR-2 along-track origin position, the j index array and the y position array are reversed).

The absolute value of the difference between the normalised reference image and the shifted normalized comparison image is then convolved with an 11×11 pixel rotationally symmetric Gaussian shaped kernel Ke_2 (similar to the one used for the initial normalisation). This results in a regional weighted mean value of the difference of the images at the displacement (u_r, v_r) at each pixel (x_j, y_k):

$$S_{M4}(x_j, y_k; u_r, v_r) = \left| R_{norm}(x_j, y_k) - C_{norm}(x_j - u_r, y_k - v_r) \right| \bullet Ke_2, \qquad (14)$$

e.g.:

$$S_{M4}(x_j, y_k; u_r, v_r) = \sum_{m=0}^{p-1} \sum_{n=0}^{q-1} \left| \left[\frac{(R - R_{Ke})(x_j + m - \frac{p}{2}, y_k + n - \frac{q}{2})}{\sigma_{M4,R}((x_j + m - \frac{p}{2}, y_k + n - \frac{q}{2})) + \varepsilon} \right] \right.$$
$$\left. - \left[\frac{(C - C_{Ke})(x_j + m - \frac{p}{2}, y_k + n - \frac{q}{2})}{\sigma_{M4,C}((x_j + m - \frac{p}{2}, y_k + n - \frac{q}{2})) + \varepsilon} \right] \right| \times Ke_2(m, n) \tag{15}$$

where the (u_r, v_r) designs the rth displacement vector in the list. This metric value is similar to the one used in the M2 matcher except for the fact that a weighted averaging is used instead of a simple average.

While working through the list of displacement vectors for each pixel position, the minimum value of the metric and the displacement values causing this minimum are stored. A first quality indicator of the disparity measures is the minimum value of the metric, which results from this process.

One should note that the estimation of the x and y disparities is often restricted to a certain window by previously setting an x and y search range.

3.4 *Rejection of bad matches*

The first step here is to exclude all edge pixels from further consideration. The width of the edge depends on the size of the kernels and the displacement vectors found within the scene.

The initial comparison image is then warped into the same position within the initial reference image using the local displacement vectors stored previously:

$$C_{warp}(x,y) = C(x - u_{x,y}, y - v_{x,y}), \tag{16}$$

where $(u_{x,y}, v_{x,y})$ is the displacement vector stored at the pixel (x,y).

As the radiometric properties of the initial reference image and the warped comparison image might differ substantially, a linear fit between the two images is determined to correct for these differences. If this difference is greater than a certain threshold value, the match is rejected. In the M4 matcher this threshold has been set equal to $2\sigma_{M4, R}$, *i.e.* twice the regional standard deviation computed for the reference image.

Note that comparison of the actual deviation of the warped image with the value of the regional standard deviation appears to reflect the complexity of the image. With highly varying image content even sub-pixel errors of the displacement can cause strong deviations, whilst in image areas with very homogeneous content, even small deviations might be a hint that something went wrong.

The M4 area-based stereo matcher is simpler to implement than some other matchers and does not require the x and y disparities (search window) to be initially set (albeit they may be set in order to constrain the search window further).

The main differences between the M4 matcher presented here and the M2 matcher can be summarized as follows:

- A local (or regional) standard deviation is used instead of the difference between the minimum and the maximum value of the BRF (or temperature) for normalization.
- A Gaussian - shape weighted, rotational symmetric patch is used rather than a square patch for normalization and the matching metric.

- The cross-correlation is calculated to cut down the number of places the matcher needs to look at in the search window.

4.   Inter-comparison of M2/M3 and M4 Stereo matcher outputs

Extensive testing was performed on all three stereo matchers (M2, M3, M4) with ATSR-2 stereo images. Initially, intercomparisons with brightness temperature values calculated from the 11μm channel were used to test whether the patch-size chosen by M4 and the grid-spacing which was pre-specified was optimum in the sense of maximising correlation between the two (see Lancaster *et al.* 2003, for more details on the justification for this approach). The results of these experiments indicated that on the one hand the single largest limitation was the pixel-level acuity in the stereo matching. On the other hand this limitation could also be considered as a strength as this was the most significant contribution to the improved speed of the matching. An example result is shown in figure 2 for ATSR-2 data acquired over the UK on 10 October 1998. This figure shows all of the input stereo channels employed at 0.65μm, 1.6μm and 11μm as red/green stereo anaglyphs (after rotating the along-track images by $90°$ to allow for stereo fusion), the resultant cloud-top heights using the matching results for M2 using the Prata camera model (for comparison, see the M4 matching results using the Mannstein camera model in figure 4 in Naud *et al.* 2007) as well as an inter-comparison of cloud-top heights derived from M2/M3 compared against M4 as a 2D scatterplot of M2-3 vs M4. Inspection of this figure shows that the stereo matching results are highly correlated. The deviation from the perfect correlation is mainly due to the pixel-level acuity in both matchers and the fact that the Prata model usually detects CTHs above those of Mannstein (see Denis *et al.* 2007 for more details). Also shown in this figure is a histogram of CTHs from the different channels and the corresponding CTH derived from brightness temperatures (CTH-Bt) not corrected for cloud emissivity effects and a 2D scatterplot of CTH-Bt compared with stereo-CTHs which shows the very different characteristics of both techniques. For a further discussion of these issues, see Naud *et al.* (2007).

5.   The impact of cloud motion on the accuracy of cloud-top heights

Seiz (2004) show an example of the effects of extreme wind resulting in a substantial cloud motion between forward and nadir scan on errors in cloud-top height retrievals and how independently derived cloud-tracked winds (when the same clouds can be identified) can be used to provide a correction for such winds in cloud-top heights. A key issue which is addressed here is how commonplace are such extreme along-track winds associated with severe weather conditions and hence cloud motion effects at the spatial resolution of ATSR-2.

   An analysis was conducted of global climate data to try to establish both the mean and anomaly over a 25 year time Period (1980–2005). Data and graphical tools from the NOAA-CIRES Climate Diagnostics Center (http://www.cdc.noaa.gov/cgi-bin/Composites/printpage.pl) were used to analyse the meridional wind fields as a proxy for the along-track component. Figure 3 shows a plot of the mean meridional windfield at 1000mb, 500mb and 200mb to try to represent the mean conditions for low, middle and high cloud respectively. Examination of these figures shows that few regions have meridional wind-fields above 5 m/sec with positive exceptions being at 200mb and 500mb (Greenland to Canada) and 1000mb
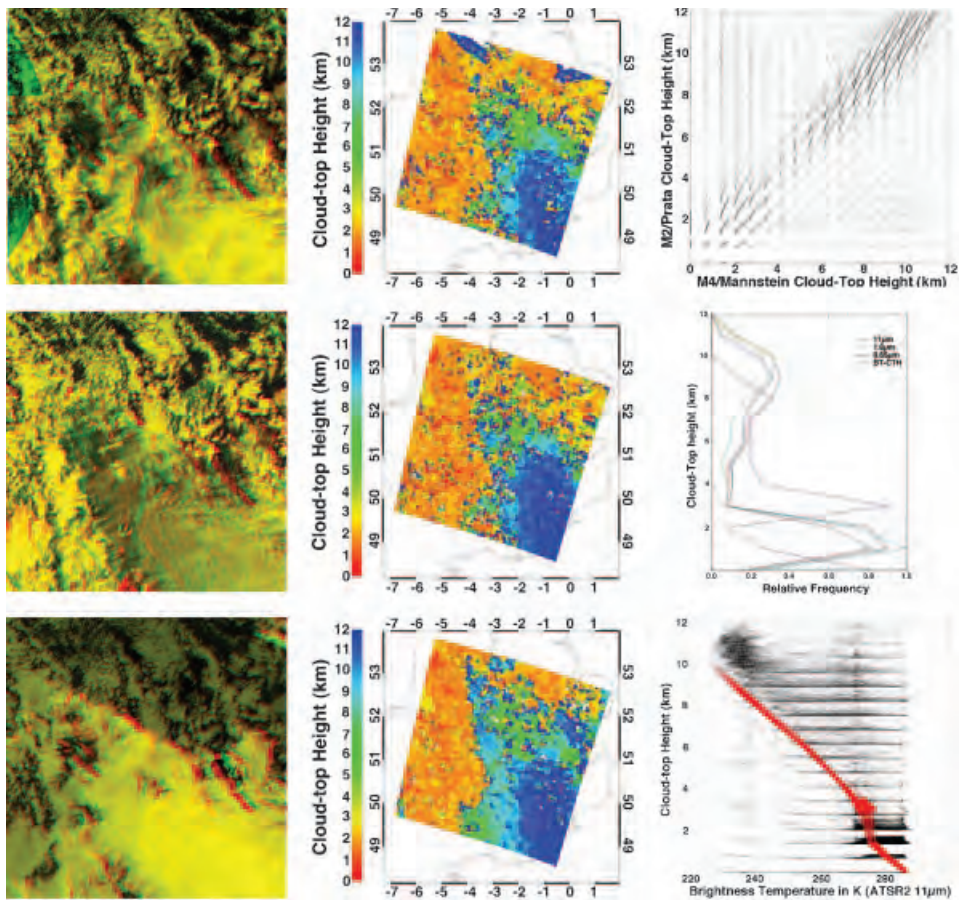
Figure 2. Stereo ATSR-2 cloud-top height (CTH) results for data acquired over the UK on 10 October 1998. Left-most column: (*a*): input 0.65μm, 1.6μm and 11μm respectively of stereo nadir + forward images as red/green stereo anaglyphs (after rotating the along-track images by 90° to allow for stereo fusion). (*b*) Middle column: M2 CTH results using the Prata camera model (Denis *et al.*, 2007). For comparison against the matching results for M4 and the Mannstein camera model see figure 4 (Naud *et al.*, 2007). (*c*) Rightmost column (from top-to-bottom): Top: 2D scatterplot of cloud-top heights derived from M2/M3 compared against M4, MIDDLE: CTH histogram for the whole scene including a brightness temperature (Bt) derived CTH, and bottom: CTH vs Bt including the CTHs derived from Bt.

(Antarctic near 180°E) and large negative anomalies over Canada, Antarctica and China. Using the equations stated in Seiz (2004) figure 4 shows the theoretical correction for a given wind speed at any CTH. Superimposed are the frequency distributions of ECMWF V-wind speed at radar CTHs for 67 and 74 cases at the US ARM Southern Great Plains, SGP (solid) and the Chilbolton Facility for Radar Research, CFARR (dashed) respectively, sampled over 640s and centered on ATSR-2 overpasses at these sites (see Naud *et al.* 2007 for more details). The top axis shows the % of the frequency of occurrence. This plot indicates that for most typical meridional wind-speeds of value ≪15 m/sec the error in CTH will be comparable to the error in the stereo camera model (Denis *et al.* 2007). Therefore for most practical purposes, this advective wind-speed error can be neglected or if a correction is required, independent objective analysis data such as ECMWF can be used.
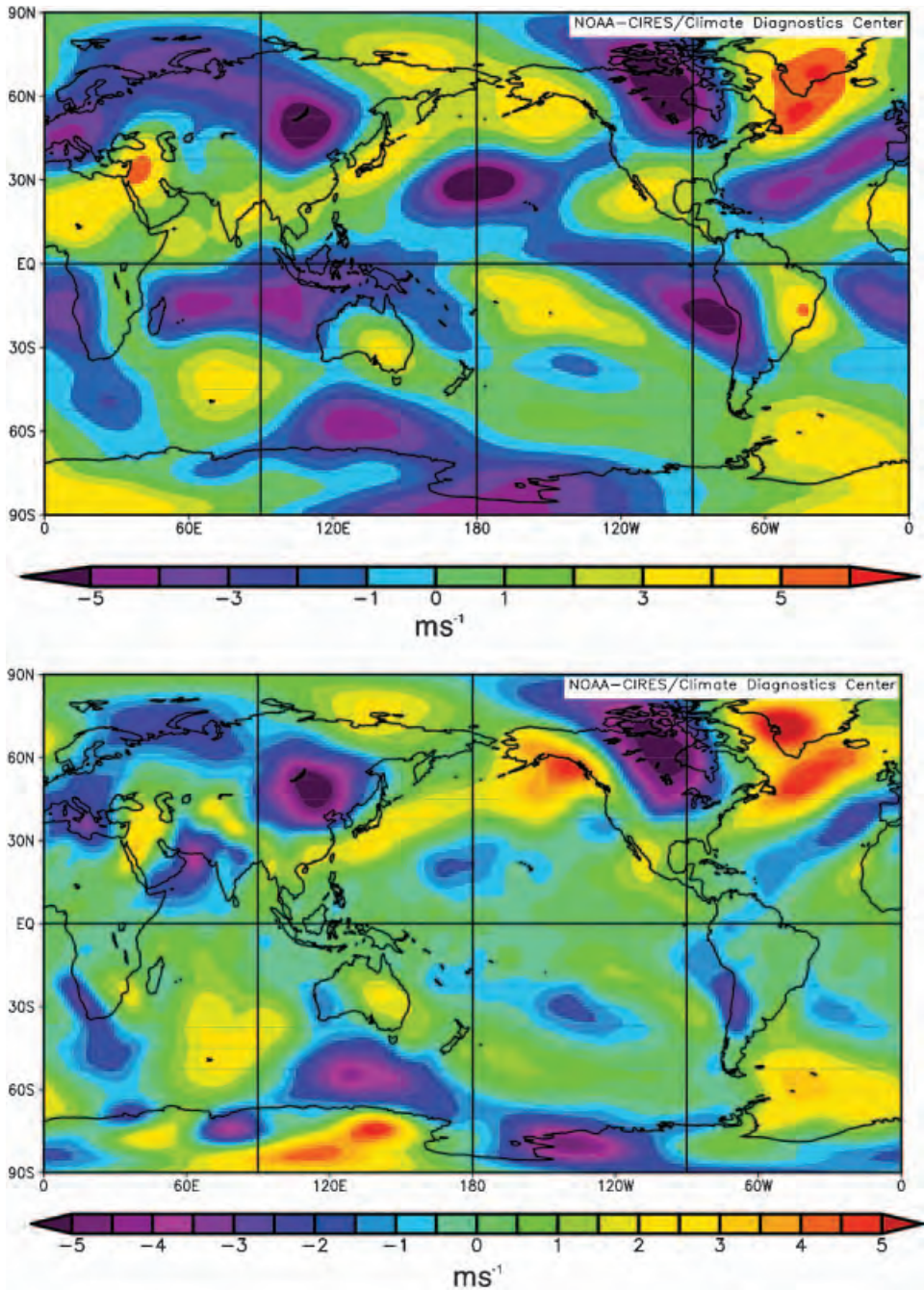
Figure 3. Mean meridional windfields in m s^{-1} at 200mb (top), 500mb (middle) and 1000mb (bottom) from 1980-2005 derived from the NOAA-CIRES Climate Diagnostics Center (http://www.cdc.noaa.gov/cgi-bin/Composites/printpage.pl) using the NCEP/NCAR Reanalysis data from January 1980 to December 2005.
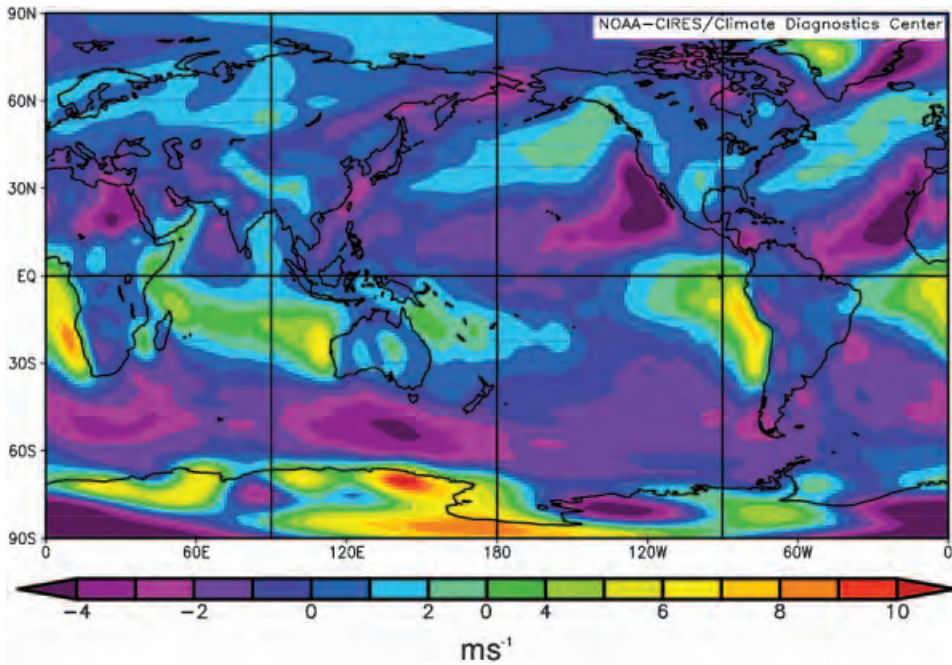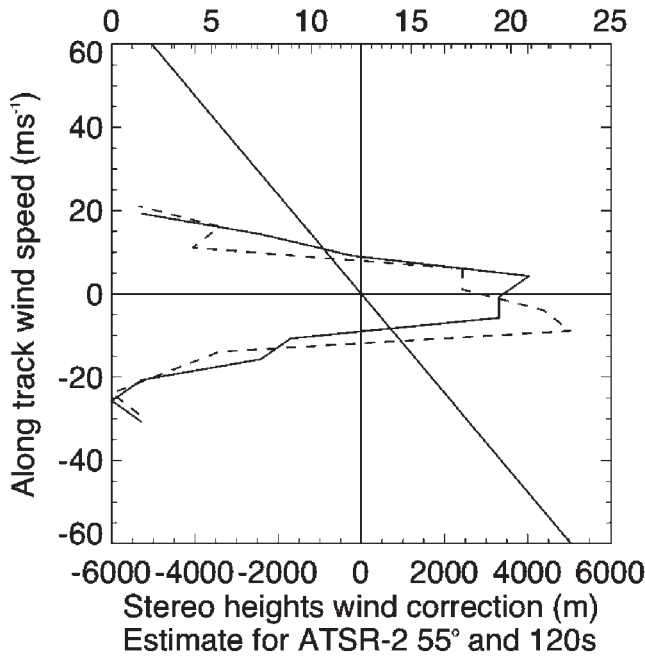
Figure 3. Continued.

Figure 4. Theoretical correction for a given wind speed at any CTH (derived using the formulations in Seiz 2004). Superimposed are the frequency distributions of ECMWF V-wind speed at radar CTHs for 67 cases at ARM-SGP (solid) and 74 cases at CFARR (dashed) respectively, sampled over 640s centered on ATSR-2 overpasses at these sites.

6.   Multispectral stereo matching for multi-layer cloud detection

ATSR-2 stereo-derived CTHs have the significant advantage over other stereo along-track medium resolution stereo sensors of sampling at visible, near-Infrared and thermal Infrared wavelengths. As each area based matcher reacts on image contrast, differences, due to the different scattering and absorption (Wylie *et al.* 1998), can be used to sample different cloud-top heights. The contrast in the visible and near-Infrared stereo-CTHs usually come from the highest optically thick dense cloud in multi-layer cloud situations. Such situations are very commonplace. The contrast in the thermal Infrared channel comes from the first and highest, often thin cirrus cloud which is usually transparent at visible/near-Infrared wavelengths. Thus ATSR-2 provides an unique potential to measure CTHs at both the upper level and a lower level when the upper layer is sufficiently thick (Naud *et al.* 2007). Unfortunately, no coincident independent measurements of cloud boundaries from space, such as lasers were available to assess a lower limit on cloud optical depth when such a situation occurs. Figure 5 shows an example of CTHs retrievals from such a multi-layer cloud situation. It is clear from this figure that the $11\mu m$ channel picks up the cirrus and contrails whereas the red ($0.65\mu m$) channel patently does not and the Near-Infrared, NIR ($1.6\mu m$) picks an area just below the upper cloud deck.

7.   Discussion and conclusions

An IDL processing chain for automated derivation of cloud-top height and amount from multispectral ATSR-2 has been described. This processing chain was delivered to our partners on the EU-CLOUDMAP2 project (http://cloudmap.org) together with the software to correct for dropped lines or other bad input data. It was used within the CLOUDMAP2 project to generate daily and monthly CTHs (http://www.cloudmap2.rl.ac.uk/results.html) and amounts for the CLOUDMAP2 area (35-80°N, 15-40°W) for a near continuous record of four years (1997–2001) when GBT data was available. In parallel to these stereo-CTH ATSR-2 products, Dr C. Poulsen at the Rutherford Appleton Laboratory, Central Council for the Laboratories of the Research Councils, CCLRC, UK has processed the same time period using an Optimal Estimation algorithm (Watts *et al.* 1998) which includes a cloud-top height product from multi-spectral analysis of the ATSR-2 data.

To extend the record back through ATSR would require rewriting much of the processing chain to handle unprojected, uncollocated nadir-forward data. Previous experience with such data has shown that a different, much slower sub-pixel matcher would then be required capable of handling this non-epipolar data (Muller *et al.* 2002). This processing chain could be modified in future with ENVISAT-AATSR data using the BEAM toolkit (http://www.brockmann-consult.de/beam/documentation.html) and the GETASSE30 (http://www.brockmann-consult.de/beam/docs/help/Tools/GETASSE30ElevationModel.html) global terrain model.

Several example results were shown to demonstrate the similar coverage and accuracy but much higher performance of M4 cf. M2/M3 as well as the potential, given certain upper level thin cloud situations, for ATSR-2 to be able to retrieve two different CTHs simultaneously. Previous work with M2/M3 (Cawkwell and Bamber 2002, Cawkwell *et al.* 2001) showed the huge potential of stereo-derived cloud fractions to produce a reliable cloud climatology over the polar regions and other regions affected by snow. Such potential could be realized worldwide with ATSR-2
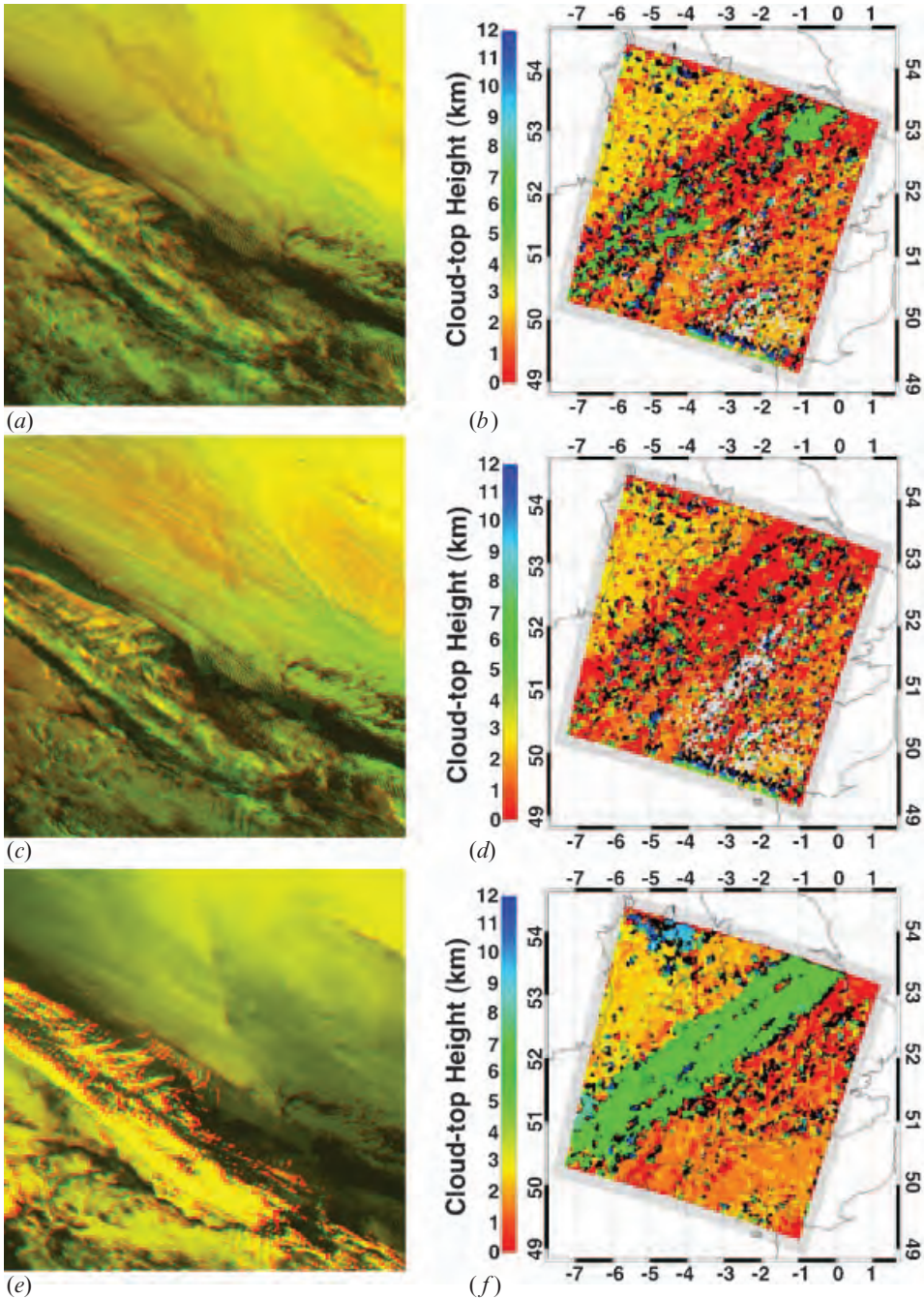
Figure 5. Stereo ATSR as a red/green stereo anaglyph (after rotating the along-track images by 90° to allow for stereo fusion). and derived cloud-top heights (CTHs) results for data acquired over the UK on 3 December 1998. (*a*) stereo anaglyph of input 0.65μm forward and nadir views; (*b*) corresponding CTH from M4 algorithm showing the detection of the lowest cloud deck; (*c*) stereo anaglyph of input 1.6μm forward and nadir views 1.6μm; (*d*) corresponding CTH from M4 algorithm showing the detection of a slightly higher cloud deck from 1.6μm stereo; (*e*) stereo anaglyph of 11μm stereo images; and (*f*) corresponding CTH from M4 algorithm showing the detection of the upper-level cirrus clouds at 11μm.

and further information gleaned from intercomparisons with radiative transfer retrievals, especially on cloud emissivities (Szejwach *et al.* 1983).

References
BLACK, P.G., 1983, Tropical storm structure revealed by stereoscopic photographs from SYLAB. *Advances in Space Research*, **2**, pp. 115–124.

CAWKWELL, F.G.L. and BAMBER, J.L., 2002, The impact of cloud cover on the net radiation budget of the Greenland ice sheet. *Annals Of Glaciology*, **34**, pp. 141–149.

CAWKWELL, F.G.L., BAMBER, J.L. and MULLER, J.P., 2001, Determination of cloud top amount and altitude at high latitudes. *Geophysical Research Letters*, **28**, pp. 1675–1678.

DENIS, M.-A., MULLER, J.-P. and MANNSTEIN, H., 2007, ATSR-2 camera models for the automated stereo photogrammetric retrieval of cloud-top heights—initial assessments. *International Journal of Remote Sensing*, **28**, pp. 1939–1955.

FUJITA, T.T., 1982, Principle Of Stereoscopic Height Computations And Their Applications To Stratospheric Cirrus Over Severe Thunderstorms. *Journal of the Meteorological Society of Japan*, **60**, pp. 355–368.

FUJITA, T.T. and DODGE, J.C., 1983, Applications of stereoscopic height computations from dual geosynchronous satellite data/Joint NASA-Japan stereo project. *Advances in Space Research*, **2**, pp. 153–160.

HASLER, A.F., 1981a, Stereographic Observations From Geosynchronous Satellites – An Important New Tool For The Atmospheric Sciences. *Bulletin of the American Meteorological Society*, **62**, pp. 194–212.

HASLER, A.F., 1981b, Stereographic observations from satellites: An important new tool for the atmospheric sciences. *Bulletin of the American Meteorological Society*, **62**, pp. 194–212.

HASLER, A.F., MACK, R. and NEGRI, A., 1983, Stereoscopic observations from meteorological satellites. *Advances in Space Research*, **2**, pp. 105–113.

HASLER, A.F., STRONG, J., WOODWARD, R.H. and PIERCE, H., 1991, Automatic-Analysis Of Stereoscopic Satellite Image Pairs For Determination Of Cloud-Top Height And Structure. *Journal of Applied Meteorology*, **30**, pp. 257–281.

HOUGHTON, J.T., DING, Y., GRIGGS, D.J., NOGUER, M., VAN DER LINDEN, P.J., and XIAOSU, D. (Eds), 2001, *Climate Change 2001: The Scientific Basis* (Cambridge: Cambridge University Press, UK), 944 pp.

KING, M.D., KAUFMANN, Y.J., MENZEL, W.P. and TANRE, D., 1992, Remote sensing of cloud, aerosol, and water vapour properties from the Moderate Resolution Imaging Spectrometer (MODIS). *IEEE Transactions on Geoscience and Remote Sensing*, **30**, pp. 2–27.

LANCASTER, R.S., SPINHIRNE, J.D. and MANIZADE, K.F., 2003, Combined infrared stereo and laser ranging cloud measurements from shuttle mission STS-85. *Journal of Atmospheric and Oceanic Technology*, **20**, pp. 67–78.

LORENZ, D., 1983, Stereoscopic imaging from polar orbit and synthetic stereo imaging. *Advances in Space Research*, **2**, pp. 133–136.

LORENZ, D., 1985, On the feasibility of cloud stereoscopy and wind determination with the Along-Track Scanning Radiometer. *International Journal of Remote Sensing*, **6**, pp. 1445–1461.

MACK, R., HASLER, A.F. and ADLER, A.F., 1982, Thunderstorm cloud-top ascent rates determined from stereoscopic satellite observations, Proceedings of 12th Conference on Severe Local Storms. Boston, American Meteorological Society, San Antonio, TX, 12–15 January, pp. 475–478.

MACK, R., HASLER, A.F. and RODGERS, E.B., 1983a, Stereoscopic observations of hurricanes and tornadic thunderstorms from geosynchronous satellites. *Advances in Space Research*, **2**, pp. 143–151.

MACK, R.A., HASLER, A.F. and ADLER, R.F., 1983b, Thunderstorm Cloud Top Observations Using Satellite Stereoscopy. *Monthly Weather Review*, **111**, pp. 1949–1964.

MAHANI, S.E., GAO, X.G., SOROOSHIAN, S. and IMAM, B., 2000, Estimating cloud top height and spatial displacement from scan-synchronous GOES images using simplified IR-based stereoscopic analysis. *Journal of Geophysical Research*, **105**, pp. 15597–15608.

MANNSTEIN, H., MEYER, R. and WENDLING, P., 1999, Operational detection of contrails from NOAA-AVHRR-data. *International Journal of Remote Sensing*, **20**, pp. 1641–1660.

MINZER, R.A., SHENK, W.E., TEAGLE, R.D. and STERANKA, J., 1978, Stereographic cloud heights from imagery of SMS/GOES satellites. *Geophysical Research Letters*, **5**, pp. 21–24.

MOSHER, F.R., 1976, Cloud height determination, Proceedings of COSPAR Symposium on Meteorological Observations from Space and their contribution to FGGE. COSPAR, pp. 201–204.

MOSHER, F.R. and YOUNG, J.T., 1983, Real-time stereoscopic applications using the GOES operational satellites. *Advances in Space Research*, **2**, pp. 173–177.

MULLER, J.-P., MANDANAYAKE, A., MORONEY, C., DAVIES, R., DINER, D.J. and PARADISE, S., 2002, MISR stereoscopic image matchers: Techniques and results. *IEEE Transactions on Geoscience and Remote Sensing*, **40**, pp. 1547–1559.

MUTLOW, C.T., ZAVODY, A.M., BARTON, I.J. and LLEWELLYN-JONES, D.T., 1994, Sea-Surface Temperature-Measurements By The Along-Track Scanning Radiometer On The Ers-1 Satellite – Early Results. *Journal of Geophysical Research-Oceans*, **99**, pp. 22575–22588.

NAUD, C., MULLER, J.-P. and CLOTHIAUX, E.E., 2002, Comparison of cloud top heights derived from MISR stereo and MODIS CO_2-slicing. *Geophysical Research Letters*, **29**, p. 1795.

NAUD, C., MITCHELL, K.L., MULLER, J-P., CLOTHIAUX, E.E., ALBERT, P., PREUSKER, R., FISCHER, J. and HOGAN, R.J., 2007, Comparison between ATSR-2 stereo, MOS O_2-A band and ground-based cloud top heights. *International Journal of Remote Sensing*, **28**, pp. 1969–1987.

NORRIS, J.R., 2000, What can cloud observations tell us about climate variability? *Space Science Reviews*, **94**, pp. 375–380.

PRATA, A.J. and TURNER, P.J., 1997, Cloud-top height determination using ATSR data. *Remote Sensing of Environment*, **59**, pp. 1–13.

PREUSKER, R., FISCHER, J., ALBERT, P., BENNARTZ, R. and SCHÜLLER, L., 2007, Cloud-top pressure retrieval using the oxygen A-band in the IRS-3 MOS instrument. *International Journal of Remote Sensing*, **28**, pp. 1957–1967.

RODGERS, E.B., MACK, R. and HASLER, A.F., 1983a, A Satellite Stereoscopic Technique To Estimate Tropical Cyclone Intensity. *Monthly Weather Review*, **111**, pp. 1599–1610.

RODGERS, E.B., MACK, R. and HASLER, A.F., 1983b, A satellite stereoscopic technique to estimate tropical Cyclone intensity. *Monthly Weather Review*, **111**, pp. 1599–1610.

ROSSOW, W.B. and SCHIFFER, R.A., 1991, ISCCP cloud data products. *Bulletin of the American Meteorological Society*, **72**, pp. 2–20.

SAUNDERS, R.W., 1988, Cloud-top temperature/height: A high-resolution imagery product from AVHRR data. *Meteorological Magazine*, **117**, pp. 211–221.

SCHIFFER, R.A. and ROSSOW, W.B., 1983, The International Satellite Cloud Climatology Project (ISCCP): The First Project of the World Climate Research Program (WCRP). *Bulletin of the American Meteorological Society*, **64**, pp. 779–783.

SEIZ, G., 2004, Ground and satellite-based multi-view photogrammetric determination of 3D cloud geometry. PhD thesis, Institute of Geodesy and Photogrammetry, ETH Zurich, June 2003. IGBP Mitteilungen, Nr. 80.

SHENK, W.E., HOLUB, R.J. and NEFF, R.A., 1975, Stereographic cloud analysis from APOLLO 6 photographs over a cold front. *Bulletin of the American Meteorological Society*, **56**, pp. 4–16.

SZEJWACH, G., SLETTEN, T.N. and HASLER, A.F., 1983, The use of stereoscopic satellite observation in the determination of the emissivity of Cirrus. *Advances in Space Research*, **2**, pp. 161–164.

TAKASHIMA, T., TAKAYAMA, Y., MATSUURA, K. and NAITO, K., 1982, Cloud Height Determination By Satellite Stereography. *Papers in Meteorology and Geophysics*, **33**, pp. 65–78.

WARNER, C., RENICK, J.H., BALSHAWI, M.W. and DOUGLAS, R.H., 1973, Stereo photogrammetry of Cumulonimbus clouds. *Quarterly Journal of the Royal Meteorological Society*, **99**, pp. 105–113.

WATTS, P.D., MUTLOW, C.T., BARAN, A.J. and ZAVODY, A.M., 1998, Study on cloud properties derived from Meteosat Second Generation Observations. EUMETSAT Report ITT no. 97/18.

WHITEHEAD, V.S., BROWNE, I.D. and GARCIA, J.G., 1969, Cloud height contouring from APOLLO 6 photography. *Bulletin of the American Meteorological Society*, **50**, pp. 522–528.

WIELICKI, B.A. and COAKLEY, J.A., 1981, Cloud retrieval using infrared sounder data: Error analysis. *Journal of Applied Meteorology*, **20**, pp. 157–169.

WYLIE, D.P. and MENZEL, W.P., 1999, Eight years of high cloud statistics using HIRS. *Journal of Climate*, **12**, pp. 170–184.

WYLIE, D.P., SANTEK, D. and STARR, D.O., 1998, Cloud-top heights from GOES-8 and GOES-9 stereoscopic imagery. *Journal of Applied Meteorology*, **37**, pp. 405–413.